Applied Physics Letters

Poling-induced inverse time-dependent microstrain mechanisms and post-poling relaxation in bismuth ferrite

Cite as: Appl. Phys. Lett. **116**, 122901 (2020); https://doi.org/10.1063/5.0002235
Submitted: 23 January 2020 . Accepted: 06 March 2020 . Published Online: 23 March 2020

Lisha Liu, Tadej Rojac, Justin Kimpton, Julian Walker, Maja Makarovic, Jing-Feng Li, and John Daniels

View Online Export Citation CrossMark

ARTICLES YOU MAY BE INTERESTED IN

Oxygen vacancies: The (in)visible friend of oxide electronics
Applied Physics Letters **116**, 120505 (2020); https://doi.org/10.1063/1.5143309

Metal-to-insulator transition in Ruddlesden-Popper-type $Sr_{n+1}V_nO_{3n+1}$ (n=1, 2) epitaxial thin films as a function of strain and VO_2 stacking layer number
Applied Physics Letters **116**, 123101 (2020); https://doi.org/10.1063/1.5136319

Ferrimagnetic semiconductor with a direct bandgap
Applied Physics Letters **116**, 122401 (2020); https://doi.org/10.1063/1.5141509

Challenge us.
What are your needs for periodic signal detection?
Watch

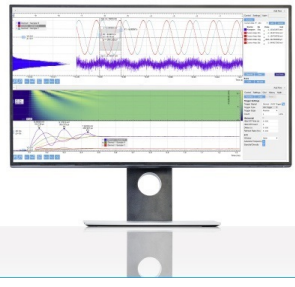

Zurich Instruments

AIP Publishing

© 2020 Author(s).

Applied Physics Letters ARTICLE scitation.org/journal/apl

Poling-induced inverse time-dependent microstrain mechanisms and post-poling relaxation in bismuth ferrite

Cite as: Appl. Phys. Lett. **116**, 122901 (2020); doi: 10.1063/5.0002235
Submitted: 23 January 2020 · Accepted: 6 March 2020 ·
Published Online: 23 March 2020

View Online Export Citation CrossMark

Lisha Liu,[1,2,a)] Tadej Rojac,[3] Justin Kimpton,[4] Julian Walker,[5] Maja Makarovic,[3] Jing-Feng Li,[2] and John Daniels[1]

AFFILIATIONS

[1]School of Materials Science and Engineering, University of New South Wales, Sydney, NSW 2052, Australia
[2]State Key Laboratory of New Ceramics and Fine Processing, School of Materials Science and Engineering, Tsinghua University, Beijing 100084, China
[3]Electronic Ceramics Department, Josef Stefan Institute, Ljubljana 1000, Slovenia
[4]Powder Diffraction, Australian Synchrotron, Melbourne 3168, Australia
[5]Materials Science and Engineering, Norwegian University of Science and Technology, 7491 Trondheim, Norway

[a)]**Author to whom correspondence should be addressed:** lishaliu@mail.tsinghua.edu.cn

ABSTRACT

Domain-wall dynamics under strong, super-coercive electric fields in polycrystalline bismuth ferrite ($BiFeO_3$) are not well established due to the experimental difficulties in processing high phase purity perovskite with low electrical conductivity. Overcoming these difficulties, here we present x-ray diffraction measurements carried out *in situ* during electrical poling with a trapezoidal electric-field to investigate the domain wall dynamics and lattice strain in this material. It is observed that during field ramping, microscopic strains, i.e., non-180° domain texture and lattice strain, increase simultaneously. During DC field dwell, however, a lattice strain decrease occurs over time, accompanied by an increase in the non-180° domain texture. This inverse time-dependent trend of microscopic strain mechanisms is speculated to be due to mobile charged defects residing in domain wall regions. The configuration of these charged point defects may also play a role in the observed post-poling relaxations of non-180° domain texture and macroscopic piezoelectric coefficients on removal of the field. Since conducting domain walls have been recently identified in a number of ferroelectrics, these results should significantly impact the understanding of strain mechanisms not only in $BiFeO_3$ but on a broader range of ferroelectric materials.

Published under license by AIP Publishing. https://doi.org/10.1063/5.0002235

Extensive applications of piezoelectrics in actuators and sensors utilize either electric-field-induced strain (converse piezoelectricity) or polarization induced by mechanical stress (direct piezoelectricity).[1] It is thus of no surprize that the strain response mechanisms in these materials are of vital importance to their functionality and have been extensively investigated. Some of the challenges include the understanding of non-180° domain switching and the associated strain that constitutes the major contribution to both the high- and low-field electromechanical properties. With potential for use in functional devices, bismuth ferrite ($BiFeO_3$) is an important lead-free ferroelectric,[2] with a large bipolar strain of 0.36% in its bulk form,[3] which is comparable to that in high-performance lead-based piezoelectric ceramics.[3,4] Previous investigations into the microscopic strain mechanism have been conducted using *in situ* x-ray diffraction (XRD),[5] observing a unipolar strain of ∼0.14% (of which ∼65% was attributed to the non-180° ferroelectric domain switching). However, it was recently found that during sub-coercive field cycling on poled $BiFeO_3$, the frequency-dependent microscopic strain mechanisms (i.e., lattice strain and non-180° domain texture) are decoupled from each other,[6] indicating a more complicated mechanism during field application in this material. Thus, further study of these mechanisms during super-coercive field application is of fundamental interest and practical importance.

In $BiFeO_3$ ceramics, a non-180° ferroelectric domain texture relaxation after poling was previously observed, ascribed to the large intergranular stresses.[5] Counterpart studies in $BiFeO_3$ thin films of polarization relaxation revealed origins from mobile space charge redistributions (e.g., oxygen vacancies).[7–12] One may expect that the relaxation of domain texture and polarization would have a significant

Published under license by AIP Publishing

impact on the macroscopic piezoelectric coefficients, particularly in view of the aging behavior, which is particularly relevant for applications. Therefore, further understanding of the microscopic and macroscopic relaxation behavior in polycrystalline $BiFeO_3$ would facilitate the establishment of poling procedures in this material, a necessity for potentially improving the piezoelectric properties of polycrystalline $BiFeO_3$ and $BiFeO_3$-based compositions. In this work, time-resolved *in situ* synchrotron XRD experiments of $BiFeO_3$ at super-coercive electric-fields were performed. Active and complicated microstructural strain mechanisms in $BiFeO_3$ during and after super-coercive electric-field application were observed and discussed.

High-purity bulk $BiFeO_3$ ceramics were prepared by the solid state method as previously reported.[13] Subsequently, the as-sintered samples were cut, thinned to ~0.3 mm, and finally polished and electroded with gold. *In situ* XRD in a reflection geometry was carried out at the Powder Diffraction (PD) beamline of the Australian Synchrotron. A monochromatic x-ray beam of energy 12.41 keV (wavelength $\lambda = 1$ Å) was used.[14] Peak profile parameters were extracted using Pseudo-Voigt fitting functions in *Igor Pro 7* from the XRD patterns.[15] The piezoelectric d_{33} coefficient was determined using a Berlincourt-type d_{33}-meter.

The as-sintered unpoled sample is refined to be a rhombohedral structure (*R3c*), with no detectable secondary phases.[16] Figure 1 shows the contour and profile patterns of the 111/11$\bar{1}$ and 200 (indices referred to the pseudo-cubic structure) peaks of as-sintered $BiFeO_3$ during the application of the unipolar trapezoidal electric-field. During the electric-field ramping from zero to approximately 8 kV/mm, the intensity ratio of 111/11$\bar{1}$ peak pairs (represented by the color scale of the reflections) shows no significant change, while the peak position of 200_{pc} peak starts to shift toward lower 2θ (indicating the development of lattice strain). 8 kV/mm corresponds to the macroscopic coercive field E_C (black solid line). At higher fields, the lattice strain continues developing until reaching the maximum field of $E_{max1} = 11$ kV/mm (red dashed line). During the static field dwell, an enhancement of 111/11$\bar{1}$ intensity ratio (indicating the development of non-180° ferroelectric domain texture) is observed, which is accompanied by a shift of the 200 peak toward higher 2θ (lower lattice spacing). The selected 111/11$\bar{1}$ and 200 line profiles [Fig. 1(b)] show the diffraction patterns at the initial (E_0), the maximum domain texture (E_{max1} and E_{max2}), and the remnant states (E_{rem}). The largest domain texture at E_{max} and the remnant domain texture as well as the lattice strain response can be seen from the 111/11$\bar{1}$ intensity interchanges and 200 peak shift and broadening, respectively.

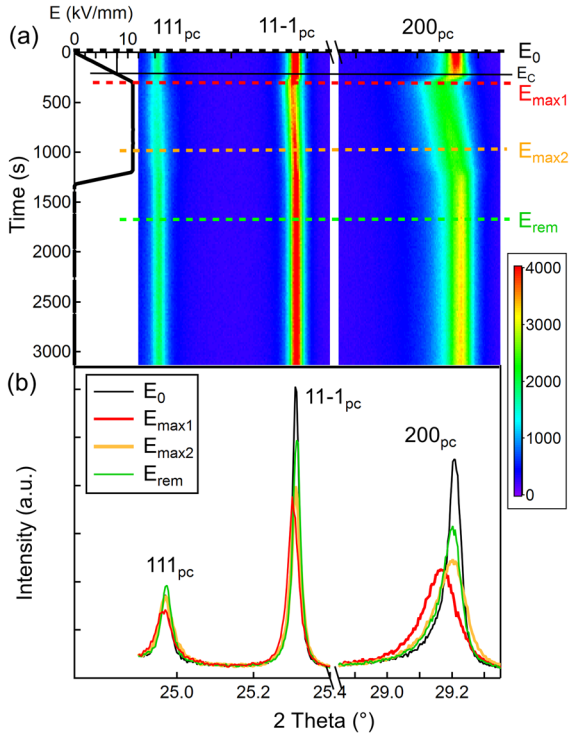

FIG. 1. Contour and line plots of synchrotron x-ray diffraction patterns during unipolar trapezoidal electric-field poling: (a) applied field profile (11 kV/mm corresponding to 1.375 E_C) and contour image of selected 111/11$\bar{1}$ and 200 peaks and (b) line plots under zero field (E_0), maximum field of 11 kV/mm (E_{max}) and shortly after field release (E_{rem}). The electric-fields at the point of interest are indicated in panel (a) by dashed lines, while the coercive field (Ec) is denoted by a solid black line.

We next quantify the non-180° domain texture and lattice strain (along the external field direction). For the domain texture analysis, we use the evolution of the integrated intensity ratios of the 111/11$\bar{1}$ peaks via the method of Multiple Random Distribution (MRD).[17] On the other hand, the shift of 200 peak position is used to characterize the lattice strain in rhombohedral systems. Details of the methods are in supplementary Note S1. Figure 2 shows the non-180° ferroelectric domain texture development during *in situ* poling at different field strengths. We can see from Fig. 2(a) that the non-180° domain texture is nearly zero before reaching the coercive field [Fig. 2(a), black arrows] and starts to develop with further ramping of the electric-field. The ceramic samples show, however, different behavior during the field dwell at different fields. At the field of 11 kV/mm (1.375 E_C), the domain texture remains stable during almost all of the field dwell period, while at 12 kV/mm (1.5 E_C) the domain texture further increases. This domain texture increase with time is enhanced at 13 kV/mm (1.625 E_C). The quantified non-180° ferroelectric domain texture, f_{111}(MRD), of the $BiFeO_3$ ceramics changes from 1 MRD (representing randomly oriented domains) to reach maximum values of ~1.39 MRD, ~1.43 MRD, and ~1.75 MRD under poling field amplitudes of 11 kV/mm, 12 kV/mm, and 13 kV/mm, respectively. As expected, the values indicate the resultant domain texture increases with an increase in the poling field magnitude.

The time evolution of the domain texture data also highlights the relaxation behavior after the electric-field was removed [Fig. 2(a)]. At the point of removing the electric-field, non-180° ferroelectric domains start to switch back and a domain texture relaxation occurs. This effect is shown in Fig. 2(b) and is similar in nature to that observed in previous work.[5] The relaxation dynamics of f_{111}(MRD) can be fitted by the exponential function in Eq. (1), where τ is the characteristic time for 111 domain back-switching

$$f(t) = f_0 + f_A * \exp\left(-\frac{t}{\tau}\right). \quad (1)$$

The domain texture data were fitted starting from the time point where the electric-field drops to 0 kV/mm as indicated by the vertical red arrow in Fig. 2(a) for the case of 13 kV/mm. The remanent f_{111}(MRD) after the full relaxation period for different field amplitudes

Published under license by AIP Publishing

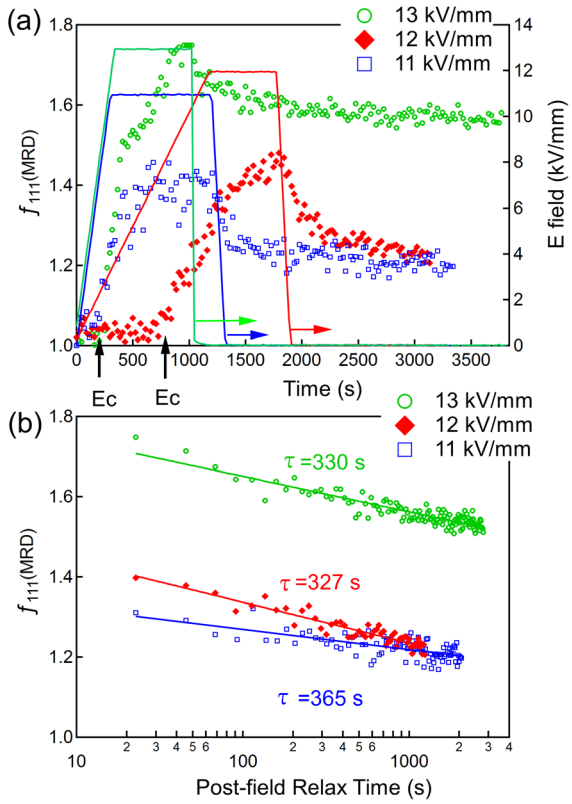

FIG. 2. 111/11$\bar{1}$ non-180° ferroelectric domain texture development during trapezoidal field poling cycle: (a) quantified multiple of random distribution (MRD) domain texture f_{111} (dots) during field ramping, constant field, and its removal as a function of time for three different maximum fields (11, 12, and 13 kV/mm). Colored full lines indicate the applied electric-field trapezoids (right vertical scale as denoted by horizontal colored arrows). Dashed lines correspond to the maximum domain texture achieved during field application. Ec is indicated for the three field ramps with black arrows; (b) post-poling relaxation after removal of the electric-field in a logarithmic timescale [τ is the relaxation time calculated using Eq. (1)]. The data were plotted from the moment the field was released as demonstrated by the vertical red arrow in panel (a) for the 13 kV/mm data set.

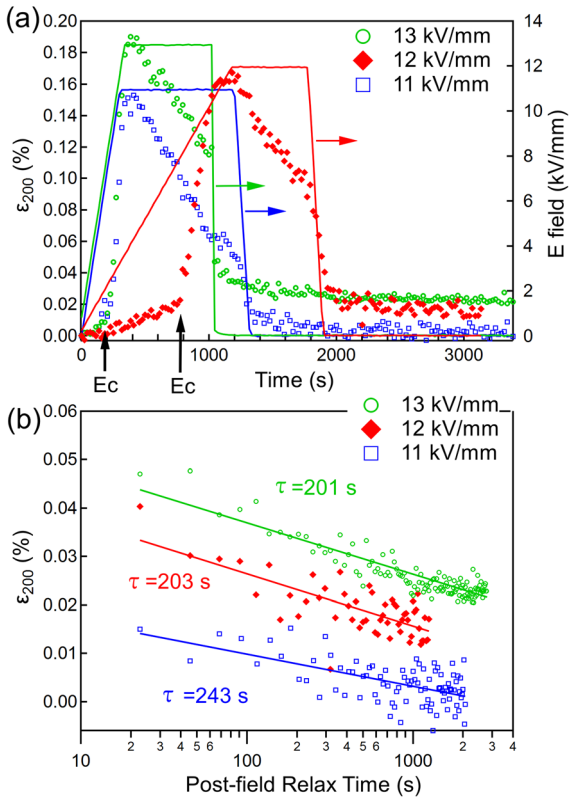

FIG. 3. Lattice-strain extracted from 200$_{pc}$ peak shifts during unipolar trapezoidal field application: (a) dashed lines correspond to the strain development during field application, while the electric-field profile with maximum field reaching 11 kV/mm (1.375 E_C), 12 kV/mm (1.5 E_C), and 13 kV/mm (1.625 E_C) is drawn by colored full lines (right vertical scale as denoted by horizontal colored arrows). Ec is indicated for the three field ramps with black arrows; (b) relaxation after removal of the electric-field [τ is the relaxation time calculated using Eq. (1)].

of 11 kV/mm, 12 kV/mm, and 13 kV/mm is 1.21 MRD, 1.23 MRD, and 1.53 MRD, respectively. Therefore, as expected, higher poling fields result in larger remnant domain texture. The relaxation time, τ, fitted for each case is similar for the three poling fields as indicated in Fig. 2(b) (in the range between ∼330 and ∼365 s).

Figure 3(a) shows the lattice strain for different field strengths as a function of time during the field application. During the initial field ramping, the lattice strain shows no obvious change before the field amplitude reaches the macroscopic coercive field [Fig. 3(a), black arrows], and then quickly increases to maxima of 0.156%, 0.162%, and 0.194% for the maximum field strengths of 11 kV/mm, 12 kV/mm, and 13 kV/mm, respectively. Immediately after reaching the maximum field, the lattice strain in all the cases starts to reduce slowly and uniformly during field holding, indicating a lattice strain release in this material. We note that this release occurs throughout the static field dwell stage regardless of the field strengths and ramping procedure, which are different in the three cases. On removal of the electric-field, the 200 lattice strain shows a sudden decrease and a further relaxation, similar to that of the domain texture, is observed. The relaxation time as fitted using Eq. (1) is ∼200 s to ∼240 s.

To understand the possible impact of domain texture relaxation (Fig. 2), post-poling small signal direct piezoelectric coefficient ($d_{33,d}$) and converse piezoelectric coefficient ($d_{33,c}$) measurements were performed on two sets of samples: (i) as-sintered samples and (ii) as-sintered samples which were subsequently heated to 900 °C (above T_C = 835 °C of $BiFeO_3$) before fast cooling (quenching) to near room temperature (herein referred to as the quenched state). Previous studies on $BiFeO_3$ indirectly confirmed that quenching leads to a transition from an ordered defect state (characteristic for as-sintered samples) to a disordered defect state (characteristic for quenched samples), which is evidenced by the transition from pinched (as-sintered) to de-pinched (quenched) polarization-field hysteresis loops.[4,18] This transition is, thus, accompanied by a release of domain walls from the ordered pinning centers and is, thus, used here to study the effect of domain wall pinning on the post-poling relaxation behavior.

The time-dependence of the piezoelectric coefficients for as-sintered and quenched samples is shown in Figs. 4(a) and 4(b), respectively. These data were obtained as a function of time immediately

Published under license by AIP Publishing

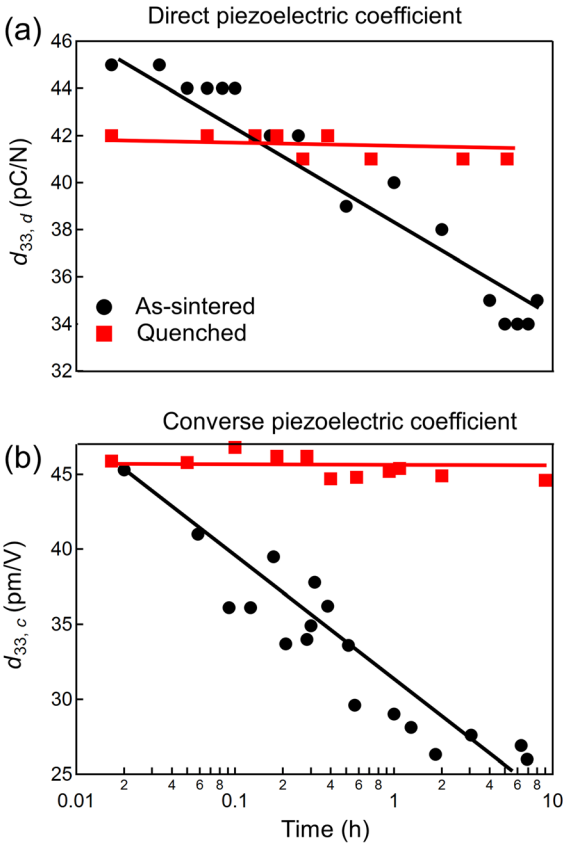

FIG. 4. Time evolution of (a) direct piezoelectric coefficients ($d_{33,d}$) and (b) converse pieozelectric coefficient ($d_{33,c}$) after removal of the poling field for as-sintered and quenched sample (both poled at 11 kV/mm for 15 min). Full lines represent fits of the datapoints using Eq. (1).

after the removal of the poling field (15 min, 11 kV/mm, 1.375 E_C) in the same way as used for the *in situ* XRD experiments. Completely different relaxation behavior of as-sintered and quenched samples, as averaged from 10 measurements in individual time-points, was observed. The as-sintered sample shows a linear decrease in both direct ($d_{33,d}$) and converse ($d_{33,c}$) piezoelectric coefficients as a function of logarithmic time after poling [Figs. 4(a) and 4(b), black dots and black curve]. This relaxation behavior can be fitted by a similar exponential form as used for the domain texture relaxation [as shown in Fig. 2(b) and Eq. (1)]. The averaged relaxation time of the direct and converse piezoelectric coefficients is ~2000 s. The origin of the difference is likely due to the different characteristics of the two experiments from which the relaxation times were determined, i.e., *in situ* XRD measurements directly quantify the variation in the domain texture with no applied field (i.e., relaxation), while measurements of the weak-field piezoelectric coefficient are affected by the switchable domain-wall contribution under the weak-field stimulus. Conversely, the piezoelectric coefficients of quenched samples stabilized at the initial values with little relaxation despite adopting identical poling procedures.

The observed relaxation of d_{33} coefficients in the as-sintered sample containing ordered defects and its absence in the quenched sample containing disordered defects suggests that the relaxation behavior is strongly influenced by defect arrangement. According to the defect chemistry models, the dominant defects in $BiFeO_3$ sintered in oxygen-rich atmosphere (for example, in air as described in this text) are oxygen vacancies, bismuth vacancies, and Fe^{4+} (oxidized states of Fe^{3+} cations).[19–23] In particular, the Bi vacancies and Fe^{4+} have been found to accumulate at domain walls,[24] provoking both the domain-wall conductivity (associated with Fe^{4+} states) and domain-wall pinning. We believe that these two features play an important role in the poling and post-poling strain behavior of as-sintered samples observed in the current study. Combining the microscopic and macroscopic experiments, we next discuss the strain mechanisms and their relationship to the defects during the different stages of external field application, i.e., field ramping, field dwell, and subsequent field removal.

During the electric-field ramping, non-180° domain walls start to move once Ec is reached and, as expected, the 111 domain texture increases with increasing maximum field applied [Fig. 3(a)]. Considering that the 200 strain of $BiFeO_3$ is a combination of the intrinsic piezoelectric strain and the deformation caused by the elastic compliance strain in response to the non-180° domain texture strain of neighboring $111/11\bar{1}$ oriented grains, the microscopic mechanisms, i.e., domain texture strain and lattice strain, show the same time-dependent behavior (i.e., they both increase with time) as expected (see e.g., Ref. 25).

During the static dwell at a maximum field, the 111 domain texture further develops [Fig. 2(a)], while the 200 lattice strain decreases [Fig. 3(a)], resulting in an inverse trend of these strain mechanisms. A similar frequency-dependent decoupling of domain texture strain and lattice strain was also recently reported during sub-coercive field cycling in $BiFeO_3$.[6] This effect was attributed to the movement of charged defects along the domain walls on application of external electric-field, which results in an internal electric-field redistribution in different grain families (e.g., {111} grains and {200} grains). According to the proposed model, this redistribution of electric-fields should enhance the domain texture strain in one grain family (i.e., with {111} orientation), while reducing the lattice strains in another grain family (i.e., with {200} orientation). We propose here that this field redistribution also operates under super-coercive field application, resulting in the inverse time-dependent microscopic mechanisms as shown in the current work. It is worth noting that this inverse trend of microscopic strains may imply interruptions of grain interactions in polycrystalline $BiFeO_3$ via micro-cracking which will be discussed further below.

On removal of the external electric-field, the domain texture is significantly relaxed, with a concurrent release of 200 lattice strain. Comparable relaxation time of these microscopic strains excludes micro-cracking as a main cause for the observed phenomena. This can be further confirmed by the scanning electron microscopic images of both the as-sintered and quenched samples after poling, both showing small amounts of microcracks (see supplementary material Fig. S1). Additionally, we argue that the relaxation behavior obtained here represents the bulk property of $BiFeO_3$ despite the result being obtained from XRD analyses in reflection mode. This conclusion is based on three observations: (1) previous studies on $PbZr_xTi_{1-x}O_3$(PZT) and $(Bi_{0.5}Na0_{.5})TiO_3$-6.25$BaTiO_3$[26] reporting comparable magnitude of responses for surface and bulk, (2) the same experiments conducted on a "soft" PZT resulted in no domain texture relaxation

Published under license by AIP Publishing

(supplementary material Fig. S2), and (3) the relaxation of piezoelectric coefficient, d_{33}, (Fig. 4) was obtained from the bulk.

The relaxation of the domain texture on electric-field removal may be explained both by "backswitching" due to residual integranular stresses induced by the poling and/or by backswitching due to the pinning effects arising from the presence of defects. In the latter case, those defects which to a first approximation show limited mobility during field application (e.g., Bi vacancies), may provoke backswitching of domains due to a domain-wall-defect pinning force. This mechanism is usually used to explain the domain switching in so-called "hard" ferroelectrics.[27] Therefore, we may expect a reduced post-poling relaxation in the quenched samples where the disordered defects provide a weaker pinning effect compared to that in as-sintered ceramics where defects are ordered. The role of defects in the relaxation of the domain texture appears as an important factor considering that negligible relaxation of macroscopic piezoelectric coefficients was observed in the quenched sample compared to the as-sintered $BiFeO_3$ (Fig. 4).

In summary, microscopic strain mechanisms of $BiFeO_3$ ceramics have been studied by *in situ* XRD combined with macroscopic piezoelectric measurements. Consistent time-dependent microscopic strain mechanisms during field ramping and inverse time-dependence on static field dwelling were observed. The relaxation of the microscopic strains and macroscopic response (d_{33}) after removal of the electric-field were also addressed. The configuration of point defects, in terms of their movements and order/disorder states, is discussed as an important factor in the strain dynamics. We show that the present results should support further studies on $BiFeO_3$ focusing on defect engineering and on the optimization of the poling conditions for future applications of $BiFeO_3$-based piezoceramics.

See the supplementary material for the quantification of the microscopic strain mechanims in $BiFeO_3$, i.e., the domain texture and the lattice strain (supplementary material note S1), the SEM images of the as-sintered and quenched samples after poling (supplementary material Fig. S1), and an anolog study of microscopic strain mechanisms in soft PZT (supplementary material Fig. S2).

J.E.D. acknowledges financial support from Australian Research Council Discovery Project Nos. DP120103968 and DP130100415. The Australian Synchrotron is acknowledged for the provision of experimental beam-time. T.R. acknowledges funding provided by the Slovenian Research Agency (Program No. P2-0105 and Project No. PR-08350) the Centre of Excellence NAMASTE for access to laboratory equipment.

REFERENCES

[1]K. Uchino, *Piezoelectric Actuators and Ultrasonic Motors* (Kluwer Academic, Boston, 1996).
[2]D. Lebeugle, D. Colson, A. Forget, and M. Viret, Appl. Phys. Lett. **91**(2), 022907 (2007).
[3]T. Rojac, M. Kosec, and D. Damjanovic, J. Am. Ceram. Soc. **94**(12), 4108–4111 (2011).
[4]T. Rojac, A. Bencan, B. Malic, G. Tutuncu, J. L. Jones, J. E. Daniels, and D. Damjanovic, J. Am. Ceram. Soc. **97**(7), 1993–2011 (2014).
[5]N. H. Khansur, T. Rojac, D. Damjanovic, C. Reinhard, K. G. Webber, J. A. Kimpton, and J. E. Daniels, J. Am. Ceram. Soc. **98**(12), 3884–3890 (2015).
[6]L. Liu, T. Rojac, D. Damjanovic, M. D. Michiel, and J. Daniels, Nat. Commun. **9**, 4928 (2018).
[7]Y.-C. Chen, G.-F. Wang, H.-H. Tai, J.-W. Chen, Y.-C. Huang, J.-C. Yang, and Y.-H. Chu, Nanotechnology **22**, 254030 (2011).
[8]Y. H. Jang, C. H. Kim, S. J. Seo, and J. H. Cho, Thin Solid Films **548**, 52–57 (2013).
[9]Y.-C. Chen, C.-H. Ko, Y.-C. Huang, J.-C. Yang, and Y.-H. Chu, J. Appl. Phys. **112**(5), 052017 (2012).
[10]J. A. Klug, M. V. Holt, R. N. Premnath, A. Joshi-Imre, S. Hong, R. S. Katiyar, M. J. Bedzyk, and O. Auciello, Appl. Phys. Lett. **99**(5), 052902 (2011).
[11]J. Wang, J. B. Neaton, H. Zheng, V. Nagarajan, S. B. Ogale, B. Liu, D. Viehland, V. Vaithyanathan, D. G. Schlom, U. V. Waghmare, N. A. Spaldin, K. M. Rabe, M. Wuttig, and R. Ramesh, Science **299**(5613), 1719–1722 (2003).
[12]Y.-C. Huang, Y. Liu, Y.-T. Lin, H.-J. Liu, Q. He, and J. Li, Adv. Mater. **26**, 6335–6340 (2014).
[13]T. Rojac, M. Makarovic, J. Walker, H. Ursic, D. Damjanovic, and T. Kos, Appl. Phys. Lett. **109**, 042904 (2016).
[14]M. J. Hossain, L. Wang, Z. Wang, N. H. Khansur, M. Hinterstein, J. A. Kimpton, and J. E. Daniels, J. Synchrotron Radiat. **23**, 694–699 (2016).
[15]See https://www.wavemetrics.com/products/igorpro/igorpro.htm, for the installation and usage of software "IGOR." This software has been used for the fitting of diffracting peaks in the current work.
[16]J. M. Moreau, C. Michel, R. Gerson, and W. J. James, J. Phys. Chem. Solids **32**(6), 1315–1320 (1971).
[17]A. Pramanick, J. L. Jones, and J. E. Daniels, J. Am. Ceram. Soc. **92**(10), 2300–2310 (2009).
[18]T. Rojac, M. Kosec, B. Budic, N. Setter, and D. Damjanovic, J. Appl. Phys. **108**, 074107 (2010).
[19]Z. Zhang, P. Wu, L. Chen, and J. Wang, Appl. Phys. Lett. **96**, 232906 (2010).
[20]N. Masó and A. R. West, Chem. Mat. **24**, 2127–2132 (2012).
[21]M. I. Morozov, M.-A. Einarsrud, and T. Grande, Appl. Phys. Lett. **104**, 122905 (2014).
[22]M. I. Morozov, M.-A. Einarsrud, and T. Grande, J. Appl. Phys. **115**, 144104 (2014).
[23]E. T. Wefring, M. A. Einarsrud, and T. Grande, Phys. Chem. Chem. Phys. **17**, 9420–9428 (2015).
[24]T. Rojac, A. Bencan, G. Drazic, N. Sakamoto, H. Ursic, B. Jancar, G. Tavcar, M. Makarovic, J. Walker, B. Malic, and D. Damjanovic, Nat. Mater. **16**, 322–327 (2017).
[25]A. Pramanick, D. Damjanovic, J. E. Daniels, J. C. Nino, and J. L. Jones, J. Am. Ceram. Soc. **94**(2), 293–309 (2011).
[26]M. J. Hossain, Z. Wang, N. H. Khansur, J. A. Kimpton, J. Oddershede, and J. E. Daniels, Appl. Phys. Lett. **109**, 092905 (2016).
[27]X. Ren, Nat. Mater. **3**, 91 (2004).

Published under license by AIP Publishing